Research Article

Pulsed laser reshaping and fragmentation of upconversion nanoparticles – from hexagonal prisms to 1D nanorods through "Medusa"-like structures

Laszlo Sajti[1,§], Denis N. Karimov[2,§], Vasilina V. Rocheva[2], Nataliya A. Arkharova[2], Kirill V. Khaydukov[2], Oleg I. Lebedev[3], Alexey E. Voloshin[2], Alla N. Generalova[2,4], Boris N. Chichkov[5], and Evgeny V. Khaydukov[2,6] (✉)

[1] AIT Austrian Institute of Technology GmbH, Wiener Neustadt, 2700, Austria
[2] Federal Scientific Research Centre "Crystallography and Photonics" Russian Academy of Sciences, Moscow, 119333, Russia
[3] Laboratoire CRISMAT, UMR6508, CNRS-ENSIACEN, Universite Caen, Caen, 14050, France
[4] Shemyakin-Ovchinnikov Institute of Bioorganic Chemistry of the Russian Academy of Sciences, Moscow 117997, Russia
[5] Institut für Quantenoptik, Leibniz Universität Hannover, Hannover, 30167, Germany
[6] Center of Biomedical Engineering, Institute of Molecular Medicine Sechenov First Moscow State Medical University, Moscow, 119991, Russia
[§] Laszlo Sajti and Denis N. Karimov contributed equally to this work.

ABSTRACT

One dimensional (1D) nanostructures attract considerable attention, enabling a broad application owing to their unique properties. However, the precise mechanism of 1D morphology attainment remains a matter of debate. In this study, ultrafast picosecond (ps) laser-induced treatment on upconversion nanoparticles (UCNPs) is offered as a tool for 1D-nanostructures formation. Fragmentation, reshaping through recrystallization process and bioadaptation of initially hydrophobic (β-Na$_{1.5}$Y$_{1.5}$F$_6$: Yb^{3+}, Tm^{3+}/β-Na$_{1.5}$Y$_{1.5}$F$_6$) core/shell nanoparticles by means of one-step laser treatment in water are demonstrated. "True" 1D nanostructures through "Medusa"-like structures can be obtained, maintaining anti-Stokes luminescence functionalities. A matter of the one-dimensional UCNPs based on direction of energy migration processes is debated. The proposed laser treatment approach is suitable for fast UCNP surface modification and nano-to-nano transformation, that open unique opportunities to expand UCNP applications in industry and biomedicine.

KEYWORDS

upconversion nanoparticles, fluoride crystals, upconversion nanorods, one-dimensional (1D) structures, laser-induced reshaping

1   Introduction

The overwhelming majority of the prominent applications of inorganic upconversion nanoparticles (UCNPs) have originated from their unique luminescent properties. UCNPs attract considerable interest in such areas, as three-dimensional (3D) display production [1], bioimaging [2–4], therapy [5–7], nano-sensing [8, 9], anti-counterfeit labeling [10, 11], solar cell design [12, 13], 3D printing [14, 15], etc. The main advantage of UCNPs, in contrast to conventional luminescent materials, is based on the UCNP exceptional structure defining the nature of the anti-Stokes luminescence. UCNPs consist of an inorganic host matrix (basically, fluoride) co-doped with lanthanide ions, acting as sensitizers (e.g., Yb^{3+} or Nd^{3+}) and activators (e.g., Er^{3+}/ Tm^{3+} or Ho^{3+}). The network of closely spaced sensitizer ions resonantly absorbs near infrared (NIR)-radiation and non-radiatively transfers the excitation energy to neighboring activator ions. Activators provide the multiple photon absorption due to their ladder-like arranged levels and emit upconverted photons. The main benefit for application of UCNPs in biological and medical areas is based on their near-infrared excitation (970–980 nm), which falls into the so-called biotissue transparency window. UCNPs demonstrate the lack of auto-fluorescence background, no photobleaching, negligible photoblinking, and sub-centimeter depth of probe detection [16].

One of the most effective host matrices, providing excellent photoluminescent upconversion properties, is hexagonal Na$_{1.5}$Y$_{1.5}$F$_6$ (referred as β-NaRF$_4$) due to the unique combination of the structural features, bandgap and phonon spectrum [17]. Various synthetic approaches, such as thermal decomposition, hydro(solvo)thermal synthesis, sol-gel processing, co-precipitation method, as well as ionic liquid-based synthesis enable preparation of high-quality UCNPs [3]. Despite significant recent advances in the synthesis of UCNPs with various architectures, the production of nanocrystals with actual one-dimensional (1D) structure is still difficult, although approaches to the growth of fluoride micro(nano)whiskers [18] and nanorods with a high aspect ratio were demonstrated [19, 20]. However, the formation of 1D-structured UCNPs has not been reported, although single-crystal 1D nanostructures have been identified as key blocks for nanoscale industry [20]. Note that the nanorods cannot be considered as 1D upconversion nanocrystals, since

---

in "true" 1D objects the energy migration between sensitizer ions must be realized in one direction strictly. The structure of the crystal matrix (e.g., β-$Na_{1.5}Y_{1.5}F_6$) and a typical doping concentration (18%–20%) of sensitizer (e.g., Yb^{3+} ions) determine the 1D upconversion object diameter, associated with several lattice parameters at high aspect ratio.

Ultra-short pulsed laser ablation of bulk materials in liquids, also including laser fragmentation, offers unique opportunities for nanoparticle generation [21, 22]. Moreover, this non-contact one-step method can be efficiently implied for modification of nanoparticle surfaces and its biofunctionalization [23]. Laser fabrication and reshaping of nanoparticles in liquids are typically applied to metal [24, 25], semiconductor [25–27], dielectric [28–30] and organic materials [31, 32], as well as to compositions in the form of nanoalloys [33]. To date, there are only a few reports related to UCNP synthesis by ns- and ps-pulsed laser ablation of a bulk target in liquids, leading to UCNP generation [34–36]. Despite the demonstration of upconversion emission, such nanoparticles possess imperfect crystallinity and size polydispersity.

Within this context, our research focuses on rational laser-induced fragmentation synthesis and reshaping of nanoparticles with anti-Stokes luminescence under NIR-excitation, aiming to design UCNPs with unique morphology and tailored optical properties. In this work, we emphasize the progress in the knowledge of interaction between ps-laser radiation and UCNPs, which leads to controlled dynamic nanotransformation from 3D to 1D luminescent structure through extraordinary "medusa"-like particles. Excellent surface and photoluminescent properties of ps-treated nanoparticles are suitable for bioapplication, in particular for visualization in aquatic organisms. Ultra-short pulse laser treatment can be considered as a next generation technology for nano-to-nano transformation representing a new direction in the synthesis of nanoparticles with predictable morphology, crystal structure and functionality.

2   Results

The results of electron microscopy measurements of as-prepared UCNPs are presented in Fig. 1. Scanning electron microscopy (SEM) and transmission electron microscopy (TEM) analyses show uniform size distribution of UCNPs. Nanoparticles have a hexagonal prism shape with the weak crown. Prism side length and height were ~ 150 and 100 nm, respectively. TEM images of UCNPs demonstrate typical for the core/shell structure contrast (Fig. 1(b)) where the core is brighter than the shell. The energy-dispersive X-ray spectroscopy (EDX) elemental mapping of yttrium and ytterbium also confirmed core/shell structure of UCNPs where the core contains Yb while the shell is Yb-free. High resolution high-angle annular dark-field scanning TEM (HAADF-STEM) image demonstrates coherent core/shell interface (Fig. 1(c)). According to the general principle of crystal growth, the most representative and common morphology for hexagonal nanostructure compounds is hexagonal prism. The nanoparticle shape was determined by its hexagonal crystal symmetry (space group $P6_3/m$, PDF # 04-011-3581). Its crown on the basis planes {0001} is formed due to anisotropy of growth rate on the prism planes during nanoparticle synthesis [37].

As-synthesized UCNPs have hydrophobic surface, which require further surface hydrophilization to adapt their properties to specific applications. Surface modification approaches are not only complicated, but also can contaminate the system with additives and precursor reaction products, which can lead to toxic effects [16, 31]. Despite progress in this field, the control over UCNP size, shape, surface properties and the development of
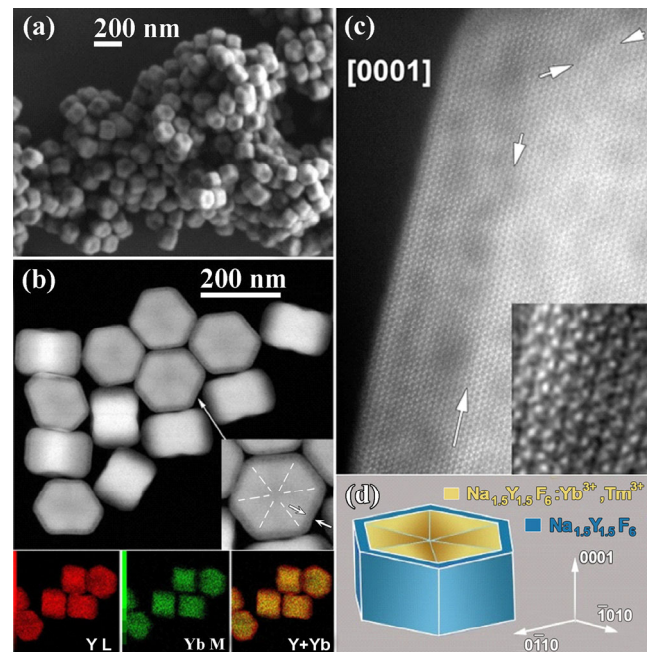

Figure 1 SEM (a) and HAADF-STEM (b) images of as-synthesized core/shell $Na_{1.5}Y_{1.5}F_6$: Yb^{3+}, $Tm^{3+}/Na_{1.5}Y_{1.5}F_6$ UCNPs featuring the β-crystal phase with mean dimensions 150 nm × 100 nm. Enlargement image of single UCNP is shown as insert. The corresponding EDX elemental mapping of Y L-line, Yb M-line and overlaid colour image for UCNPs are presented in the bottom panel; (c) high resolution HAADF-STEM image of core/shell interface; (d) schematic nanoparticle illustration, representing hexagonal crystal structure.

overall reproducible method for synthesis of colloidal stable UCNPs still remain a challenge [38].

As-prepared UCNPs were stabilized in water under ps-laser treatment. Figures 2(a) and 2(b) show the scheme of experimental setup and the image of fabrication process. Stable aqueous colloids have been formed after 1-min laser treatment of UCNPs in the presence of dye DY-631. Apparently, stabilization of the nanoparticles occurred due to substitution of oleic acid on UCNP surface by the dye molecules during laser irradiation with high-intensity pulses. The dye contains sulfo-group, which determines the surface activity of anionic surfactant [39]. Besides, the dye has the carboxyl group capable of coordination with metal ions on UCNP surface. Thus, the implication of dye DY-631, widely used in proteomics, makes it possible to replace conventional surfactant, such as sodium dodecyl sulfate, that causes cell lysis and protein denaturation. After laser treatment, the UCNP aqueous colloids remained stable for at least 5 weeks with unchanged photoluminescent properties. This new non-contact one-step approach has, therefore, great potential for fast UCNP bioprobe formation.

HAADF-STEM analysis demonstrated that 1-min ps-laser treatment induced the formation of the spherical nanodroplets originating from the UCNPs surface and having particle size distribution from 1 to 50 nm. At the same time the shape of initial UCNPs remains practically unchanged (see Figs. 2(c) and 2(d) and Fig. S1 in the Electronic Supplementary Material (ESM)).

We suppose that spherical nanodroplets were formed as a result of initial UCNP surface overheating and the injection of the molten material into the solution. Evolution of UCNP surface morphology under 1-min laser treatment demonstrates in Fig. S2 in the ESM. Initially, smooth UCNP surface was transformed into rough one, while nanoparticle composition and core-shell structure did not change after 1 min of laser
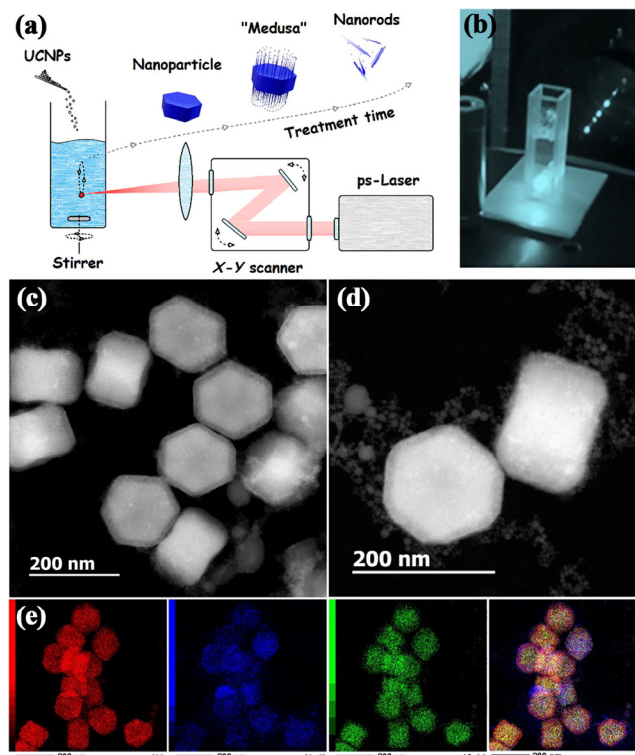
Figure 2 The scheme of experimental setup for laser reshaping and fragmentation of upconversion nanoparticles (a) and the image of fabrication process (b). HAADF-STEM images of the sample after 1 min of laser treatment (c) and UCNPs surrounding by nanodroplets (d); EDX elemental mapping of Y L-line (red), Na K-line (blue), Yb M-line (green) and overlaid colour map (Y&Na&Yb) of UCNPs (e).

treatment according to EDX elemental analysis (Fig. 2(e)).

We observed that the increase in the exposure time of ps-laser treatment provided surface modifications of UCNPs. Under ps-laser treatment for up to 5 min, the nanowhiskers were formed on the {0001} surface of the nanocrystals (Fig. 3) with a typical size of 5–10 nm in diameter and ~ 100 nm in length. It is noteworthy that the number of nanodroplets increases significantly.

Furthermore, elongated drop-shaped nanoobjects such as "Prince Rupert's drops" were also observed (Fig. S3 in the ESM). These nanostructures were probably formed due to the melt injection from the laser exposure region into the "cold" zone and following quenching in the water. With a further increase of the ps-laser treatment time up to 10 min, the nanowhiskers directly grew from the UCNP base surfaces along <0001> axes, forming structures similar to "medusa". Most of the observed nanoparticles had the same "medusa"-like structure after 10 min of ps-laser treatment (Fig. S4 in the ESM). Nanowiskers had a diameter of 5–10 nm and a length
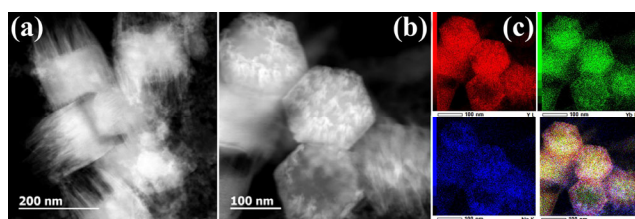

Figure 3 HAADF-STEM images of modified UCNPs after 5 min of laser treatment along two orthogonal directions: (a) close to $[10\bar{1}0]$ and (b) close to [0001] zone axis; (c) EDX elemental mapping of Y L-line (red), Yb M-line (green), Na K-line (blue), and overlaid colour map (Y&Na&Yb) of UCNPs.

of up to 300 nm (Fig. 4). Selected area electron diffraction (SAED) pattern taken from area B (Fig. 4) shows that the nanowhisker crystal structure is identical to the structure (area A) of initial hexagonal nanoparticles (space group $P6_3/m$). Elemental analysis indicates an excess of sodium fluoride, which was easily removed by purification using water, followed by centrifugation (Fig. S5 in the ESM). Note that the transformation of initial nanoparticles is accompanied by significant decrease of the base surface areas {0001}, while the size along the <0001> direction varies slightly, and whiskers fill about 30% of UCNP base surface (Fig. S6 in the ESM).

The increase of laser treatment up to 30 min leads to destruction of the "medusa"-like structures, and most of the whiskers turn into individual nanorods (Fig. 5). Detailed HAADF-STEM analysis and simultaneously acquired EDX elemental mapping demonstrate that the chemical composition (Fig. 5(b)) and crystal structure (Fig. 5(c)) of the nanorods are similar to the initial hexagonal UCNPs, which confirms the congruent transformation. Spherical nanodroplets, formed in the process of laser treatment, correspond to cubic phase (space group $Fm\bar{3}m$) with the lattice parameter $a = 0.547(1)$ nm. It is noteworthy that "Prince Rupert's drops" nanostructures were not detected in the samples after 30 min of ps-laser treatment. The destruction of nanorods and massive formation of nano-droplets is observed after continued further treatment time up to 60 min (Fig. S7 in the ESM).

The growth rate of nanowhiskers can be estimated from the experimental data analysis. We found that the whisker growth rate at the used laser parameters was constant ~ 10 nm/min, and the length increased linearly depending on laser treatment time. Taking into account the whisker density on the nanoparticle base (0001), its icicle form (average ratio of the diameter at the bottom to top is 2:1) and the hexagonal prism morphology of the initial nanoparticle, the maximal length of whiskers can be evaluated. Since the thickness of nanoparticle was approximately 100 nm, the maximal length of the grown whiskers would be 500 nm. In the experiment, nanorod length was estimated at 300 nm, which indicated that the remaining mass (~ 30%–40%) of the initial nanoparticle was spent on spherical nanoparticles formation.

Anti-Stokes luminescence behavior of morphologically diverse structures synthesized under laser treatment (nanoparticles, "medusa"-like structures and crystal nanorods) were studied. Figure 6 shows the normalized photoluminescence (PL) spectra of the nanostructure aqueous colloids after 1-, 10- and 30-min of laser treatment. The spectra contain typical Tm^{3+} ion transitions
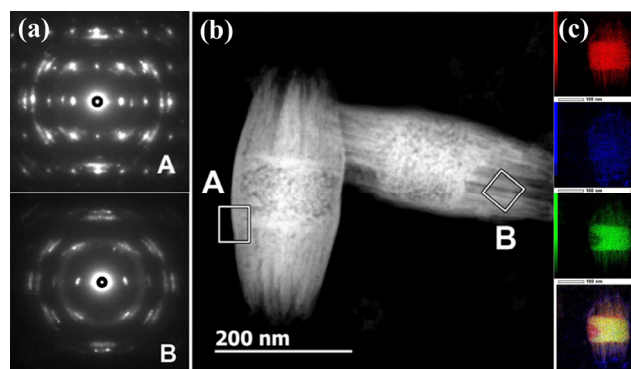

Figure 4 SAED patterns (a) taken from single modified UCNP after 10-min of laser treatment: along $[2\bar{1}\bar{1}0]$ zone axis taken from A (nanoparticle) and B (nanowhiskers) areas marked in HAADF–STEM image (b) with low magnification of "medusa"-like nanostructures; (c) EDX elemental mapping of Y L-line (red), F K-line (green), Na K-line (blue) and overlaid colour map (Y&F&Na).
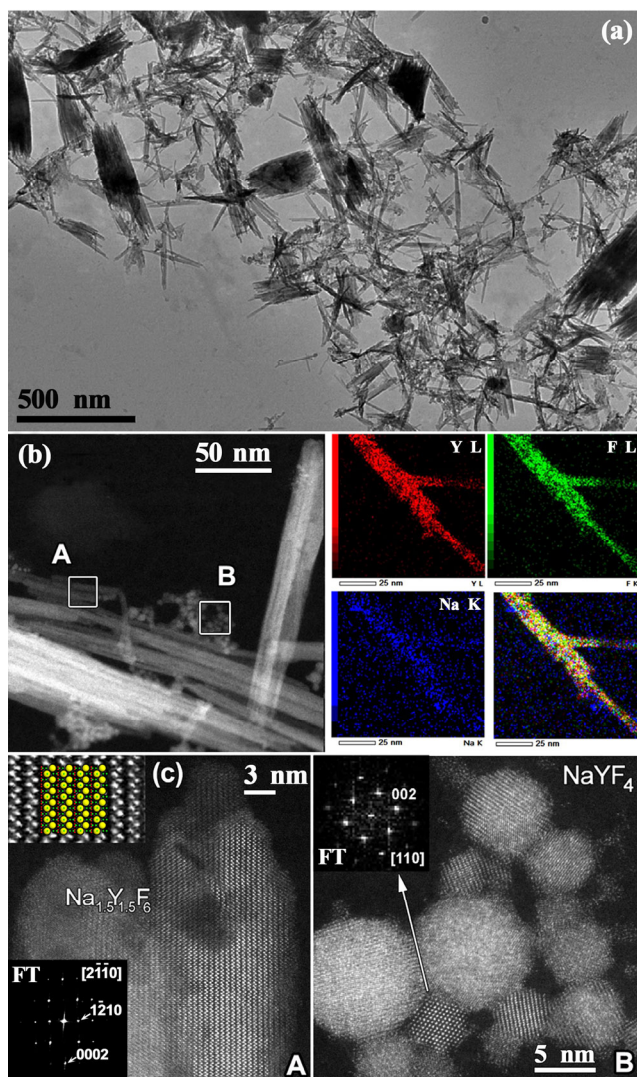
Figure 5 Bright field TEM overview image (a) of modified UCNP sample after 30-min of laser treatment with low magnification; (b) low magnification HAADF-STEM image and simultaneously acquired EDX elemental mapping of Y L-line (red), F K-line (green), Na K-line (blue) and overlaid colour map (Y&F&Na); (c) high resolution HAADF-STEM images of areas marked in (b): A – single $Na_{1.5}Y_{1.5}F_6$ nanorod (FT pattern and structural model overlaid on enlargement image is given as insert. FT pattern is indexed on $P6_3/m$ structure), B – nanodroplets of cubic $NaYF_4$ and corresponding FT pattern of single nanoparticle taken along [110] zone axis.

(Fig. 6(a)) and PL properties of nanostructures are the same in the case of continuous wave excitation at 975 nm.

The luminescence kinetics study at pulse excitation in nanoparticles vs. nanorods illustrates the complexity and significance of UCNP photophysics indicating a key role of energy migration between Yb^{3+} ions in the upconversion process. The energy migration processes in UCNPs can be demonstrated by the exploration of the spectra and kinetics of anti-Stokes luminescence. We used the excitation pulses with the duration of 1 ms at a constant repetition rate of 50 Hz, with excitation pulse fall time about 10 μs. The power density of exciting radiation was recorded in the course of kinetics measurements at 5 W/cm². In the case of pulse excitation, the PL properties of nanostructures changed dramatically (Figs. 6(d)–6(f)). After the excitation pulse termination, the energy migration between Yb^{3+} ions plays the dominant role in the upconversion process. The most likely process in the system has become the non-radiative energy transfer from Yb^{3+} to Tm^{3+} ions. Since each Tm^{3+} ion is surrounded by many excited Yb^{3+} ions, the chance

of multiphoton processes is maximal. As a result of Yb^{3+} deexcitation, each Tm^{3+} ion provides a local minimum in the spatial distribution of the accumulated energy in the system of Yb^{3+} ions. The details of the energy migration processes in UCNPs were discussed by us [40]. In the case of the 3D structure (corresponds to 1-min laser treatment), we found varying delay time of signal rise for different Tm^{3+} transitions and observed time shift of luminescent maxima. In the case of the 1D structure, the non-radiative excitation from Yb^{3+} to Tm^{3+} is limited by one direction. This leads to a scenario where the chance of upconversion process becomes lower. As a result, the PL kinetics maxima of different PL lines are shifted to excitation pulse in comparison with 3D nanostructure. "Medusa"-like structures are characterized by superposition of PL kinetics for 1D and 3D ones.

The axial and lateral cross sections of β-$Na_{1.5}Y_{1.5}F_6$: Yb^{3+}, Tm^{3+} nanorod crystal structure with atom positions is shown in Fig. S8 in the ESM. Rare earth cation occupy mixed Wyckoff position: 2d with Na^+ cation in the structure. The minimum distance R_1 between the rare earth cations is realized in the [0001] direction. At nanorod diameter ~ 3.6 nm and typical doping level the number of Yb^{3+} ions, on average, 1.8 per rare earth layer along [0001] direction is realized. On an average Tm^{3+} ions are found in every 18 such layer. This fact limits the energy migration in the base plane as the network of sensitizer ions is realized only in the [0001] direction. Therefore, the "true" 1D upconversion structure is forming at a diameter less than 4 nm.

Note that the synthesized structures with complex architecture have important properties. We speculate that "medusa"-like nanostructures can be utilized to increase the efficiency of non-radiative energy transfer. It is known that the efficiency of the Förster energy transfer is inversely proportional to the sixth power of the distance between the donor and the acceptor. The efficiency of this process is enhanced by enlarging the surface area of nanoparticles having a complicated structure, since more surface-active sites are involved in transfer process. In addition, the proposed technology lacks the surface modification step, although UCNP biocompatibility and stabilization in aqueous solutions are achieved. As a result, the one-stage laser treatment approach provides the design of nanoagents for biovisualization and therapy.

In order to demonstrate the excellent photoluminescence and hydrophilicity of synthesized complex nanoparticles, we presented their biovisualization in aquatic organisms (Fig. 7). Daphnids (*D. magna*) were exposed to "medusa"-like nanostructures in water with final concentration of 0.01 mg/mL. Accumulation experiments were performed at room temperature with a natural light–dark cycle. After 1 h-incubation, 5 organisms were analyzed microscopically in water microdroplet placed on the slide. Another 10 daphnids were transferred to fresh culture medium for depuration. After 24- and 48-h of depuration, the UCNP content in daphnia was acquired. No mortality of aquatic organism was observed. Home-built epi-luminescent upconversion microscope with excitation at 975 nm-laser light was used for UCNP visualization at 800 nm. *D. magna* was found to ingest UCNPs from water, followed by accumulation in the intestines. After 24 h of depuration, the photoluminescent signal dramatically reduces. Aquatic organism after 24-h depuration at 10 times higher gain of epi-luminescent image is shown in Fig. S9 in the ESM. *D. magna* excreted practically all ingested UCNPs and no luminescent signal was detected after 48-h of depuration. Complete UCNP excretion from the aquatic organisms indicates a lack of ecotoxicity [41], demonstrating the successful synthesis of bioagents with excellent luminescent properties.
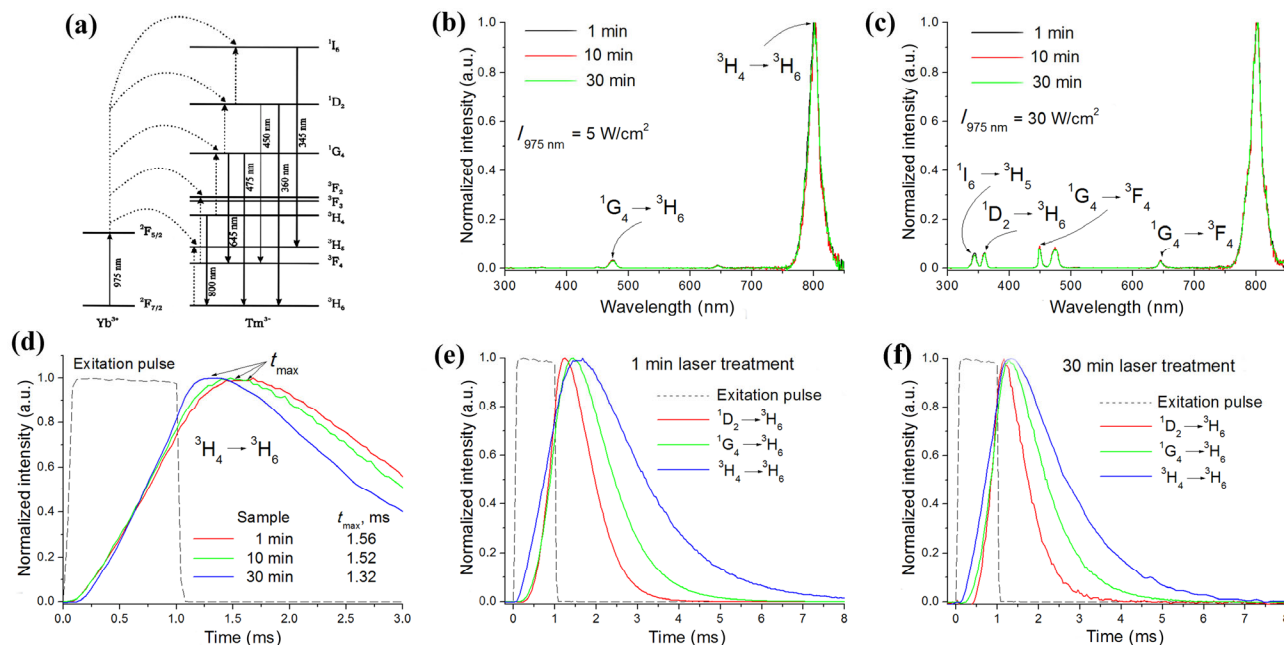
Figure 6 An energy level diagram with the main transitions of Yb³⁺ and Tm³⁺ ions in UCNP (a). The PL spectrum of the upconversion structures measured under 975 nm-continuous wave laser excitation with 5 W/cm² (b) and 30 W/cm² (c) intensity. The luminescence kinetics at 800 nm, demonstrating the substantial differences in the rise and the maxima times, which correspond to various upconversion nanostructures (d). The time dependence of the luminescence of the Tm³⁺ transitions (800 nm – blue, 475 nm – green, 360 nm –red curves) under the pulsed excitation at 975 nm for nanostructures after 1-min (e), and 30-min (f) of ps-laser treatment. The exciting pulse duration is 1 ms (black dash curve). All signals are normalized to unity. The beginning of the time scale corresponds to the exciting pulse start.
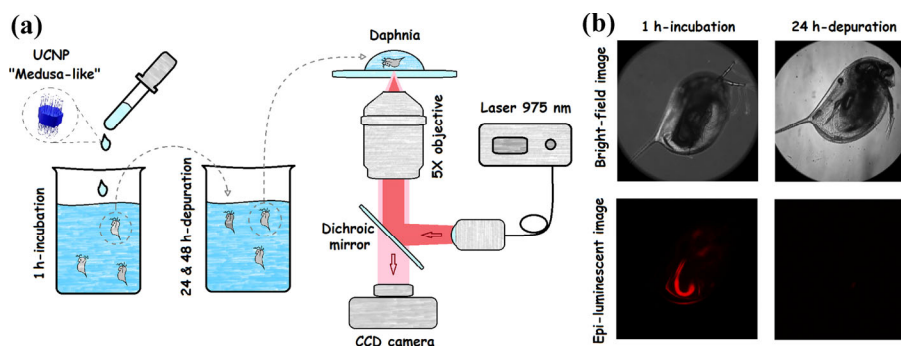

Figure 7 The scheme of aquatic organism experiment (a). Bright-field and UCNP assisted epi-luminescent images of *D. magna* after 1 h-ingestion of "medusa"-like structure and after 24 h of depuration (b).

3 Discussion

The compound NaRF₄ (R–rare earths) is dimorphic (Fig. S10 in the ESM shows the phase diagram of NaF-YF₃) [42]. The polymorphic transition from hexagonal to cubic phase is fixed at ~ 950 K for bulk material. The high-temperature phase α-NaRF₄ of variable composition has a cubic structure (CaF₂-type, space group $Fm\bar{3}m$, $Z = 4$). At the temperature decrease, the fluorite α-NaRF₄ phase decomposes according to the eutectoid scheme with the release of a low-temperature hexagonal β-Na₁.₅R₁.₅F₆ phase (NaCaYF₆ gagarinite-type structure, space group $P6_3/m$, $Z = 1$) [43]. The α-NaRF₄ phase is metastable and can be obtained from the melt in the form of bulk single crystals without their decomposition upon cooling to liquid nitrogen temperature [44]. Due to the extreme conditions associated with shock overheating of liquid at ps-laser treatment, the β-Na₁.₅Y₁.₅F₆ phase nanoparticle is separated from the initial nanoparticle surface in the molten state and is quenched in the cold liquid surrounding. This effect leads to the formation of nanometer-sized molten droplets and «Prince Rupert's» drops in the metastable cubic α-phase. Such transformation from β to α phase results in changing the chemical composition and

producing free sodium fluoride in solution, which is confirmed by phase equilibrium, as well as by XRD and TEM analysis. Melt formation in the experiments enables us to estimate the nanoparticle surface temperature under ps-laser treatment not less than 900 K. This corresponds to the eutectic point and was previously detected in experiments with inertial heating of nanoparticles [45]. Under ps-laser treatment, the crystal lattice is heated on a picosecond time scale [46], which is responsible for the enormous temperature gradient in nanoparticles. The thermal diffusivity for Na₁.₅Y₁.₅F₆ is 10⁻⁶ m²/s [47], and for water it is an order of magnitude lower. In this case, the heat flux is directed into the nanoparticle. As a result, the melt recrystallization on the nanoparticle surface determines the growth of crystalline whiskers. The convex shape of the nanowhisker tips also indicates that the heat flux is directed to the nanoparticle.

The whisker growth is observed only on the close-packed base surfaces {0001} of the nanoparticles. At a melt temperature ~ 950 K the equilibrium solid phase is fluorite. As it is known, the best conjugation of the hexagonal and cubic lattices at heteroepitaxy is achieved at the orientations of (111) cubic crystal and (0001) hexagonal crystal. However, this layer may

be too stressed, and then an island structure is formed on the surface, which gives rise to the growth of nanowhiskers. In this case, the hexagonal structure of the whiskers seems to be stabilized by the nanoparticle surface, and homoepitaxial growth is observed. On the lateral faces of the nanoparticle, the mismatch between the cubic and hexagonal lattices is much greater, which suppresses the nucleation of the islands. Therefore, whisker structure formation is not observed on the lateral plans $\{01\bar{1}0\}$ upon subsequent ps-laser pulses. These surfaces are melted and aligned owing to melt material outflow onto the base planes of the nanoparticle. The increase in the treatment time causes the nanowhisker growth due to the redistribution of the nanoparticle donor material. The whisker growth stops when the donor material of nanoparticle is exhausted, and as a result, the complex structure disintegrates into individual nanorods.

Note that the micron-sized "medusa"-like structures for $Na_{1.5}Y_{1.5}F_6$ crystals were reported [48], although their growth mechanism was obviously different, since particle production was determined by varying the component concentration in hydrothermal synthesis. An analysis of literature revealed the similar "medusa"-like structures [36], initiated by nanosecond ablation of 18%Yb:1%Er: $NaYF_4$ pellets in water, but the authors did not pay attention to these structures, since they focused on nanoball synthesis. The retention of nanowhisker core-shell structures at the initial stage of their growth (Fig. S11 in the ESM) proves the melt mechanism of their formation and excludes the mechanism of donor material resputtering, typical for ablation process.

The change in the UCNP structure, depending on the ps-laser treatment time, can be observed according to the XRD analysis (Fig. S12 in the ESM). Indeed, the phase composition remained unchanged for 5 and 10 min of laser treatment, the lattice parameters of nanostructures were modified. For initial nanoparticles, we determined hexagonal lattice parameters as $a = 0.59807(1)$ and $c = 0.35084(2)$ nm, while lattice parameters for treated nanostructures were $a = 0.59521(5)$ and $c = 0.35249(8)$ nm. This indicates that structure of initial nanoparticle slightly elongates under laser treatment. Intense XRD reflections for NaF phase ($a = 0.4633(1)$ nm), detected in the pattern after 60-min laser treatment, indicate the transformation from β to α phase of nanoparticles, which is accompanied by free sodium fluoride formation in the aqueous solution.

It should be noted that a wide variety of approaches for colloidal syntheses of 1D nanostructures have been proposed. Typically, in the course of colloidal synthesis, the atoms generate, as a result of the reduction and/or decomposition of a precursor, and then they are agglomerated to form nuclei or seeds and precipitated onto the preformed seeds. Alternatively, the seeds can assemble through an oriented attachment. Thus, two main growth pathways for the 1D nanostructure generation can be defined: atomic addition and oriented attachment [49, 50]. These pathways can be realized only in the case of an anisotropic shape of seeds, which is difficult to force during a colloidal synthesis. The symmetry breaking remains a major challenge in production of controlled 1D nanostructures. Our laser treatment approach lacks these weak points.

4   Conclusion

The process of picosecond-pulsed laser ablation in liquids is adopted to fabricate novel upconversion nanostructures with unique morphology and tailored optical functionalities. This new non-contact, one-step laser treatment approach has a great

potential for the fast UCNP hydrophilization. Prolonged ps-laser treatment partially fragmentates the initially hexagonal UCNPs to the nanodroplets (cubic phase) with ~ 1 nm diameter. We demonstrate that ps-laser treatment leads to UCNP reshaping, which results in "medusa"-like structure with complex morphology, turning into "true" 1D upconversion nanocrystals. Crystal nanorods and nanoparticles possess the identical anti-Stokes luminescence under cw-excitation at 975 nm, whereas luminescence kinetics study at pulse excitation illustrates the UCNP photophysics complexity indicating a significant role of energy migration in upconversion process. The proposed approach enables the production of 1D nanostructures with high rate and yield, which makes a start to a new competing technology for synthesis of key elementary blocks and new structures for nanoindustry. Ultrashort-pulsed laser technology can be considered as future finely customizable tool for modifying both the surface and bulk of dielectric nanoparticles that can provide progress in our knowledge of the upconversion phenomenon and expand UCNP applications in industry and biomedicine.

5   Experimental section

5.1   UCNP synthesis

All chemicals were purchased from Sigma–Aldrich (Germany). The synthesis of lanthanide doped β-$Na_{1.5}Y_{1.5}F_6$ UCNPs is based on the metal trifluoroacetate precursor thermolysis in a solution of oleic acid and octadecene, which was carried out under heating in an oxygen-free atmosphere. The details of UCNP synthesis were described by us earlier [51]. The synthesis products are hydrophobic monodisperse nanoparticles with a core/shell structure (β-$Na_{1.5}Y_{1.5}F_6$: Yb^{3+}, Tm^{3+}/β-$Na_{1.5}Y_{1.5}F_6$), capable to form stable colloids in non-polar organic solvents.

5.2   UCNP laser hydrophilization-defragmentation

Synthesized UCNPs were hydrophilized by picosecond laser pulses. Nanoparticles β-$Na_{1.5}Y_{1.5}F_6$: Yb^{3+}, Tm^{3+}/β-$Na_{1.5}Y_{1.5}F_6$ were placed in an aqueous solution of the dye DY-631 [52], which appeared to be an effective surfactant containing hydrophobic moiety and hydrophilic sulfo-groups. UCNP colloidal con-centration was 10 mg/mL. Laser pulses with duration of 7 picosecond at the wavelength of 1,030 nm from a solid-state laser system TruMicro 5250 (Trumpf GmbH, Germany) were focused in cuvette filled with UCNPs. At pulse energy 200 μJ and a pulse repetition rate of 200 kHz, laser processing of nanoparticles was performed for 1, 5, 10, 30 and 60 min. Galvano-mirrors system HurrySCAN II-14 (Scanlab AG, Germany) provided the closed loop movement of the laser beam along the surface of the quartz cuvette leading to uniform dispersion treatment. A magnetic stirrer was also used. The UCNP shape modifications were detected after laser processing from 1 to 60 min.

5.3   Luminescence kinetics measurements

In order to register spectra and kinetics of nanoparticles photoluminescence (PL), we used the Fluorolog-3 fluorometer (HJY, France), equipped with the Hamamatsu photomultiplier tube R929P (Hamamatsu Photonics, Japan). The photomultiplier tube signal was recorded with the high speed Tektronix oscilloscope TDS 6804B (Tektronix Inc, USA). In the course of PL lifetime measurements, the spectral width of the monochromator was chosen in accordance with the width of the transition under the study. A semiconductor 976 nm laser (Thorlabs, USA) was used as an excitation source.

5.4 X-ray diffraction analysis

XRD analysis was performed on a powder diffractometer Rigaku Miniflex 600 (Rigaku, Japan) with Cu Kα radiation (λ = 1.54178 Å). The measurement was carried out using the coupled scan in region 10°–120° in 2θ. Phase compositions were identified using the ICDD PDF-2 (2014). The unit cell parameters were calculated by the Le Bail full-profile fitting (the Jana2006 software).

5.5 Electron microscopy

The SEM was performed on a Scios (FEI, USA) at 5 kV using secondary electron detector (Everhart-Thornley detector) in Optiplan mode.

The TEM, including electron diffraction, HAADF-STEM and simultaneously acquired the EDX elemental mapping analysis were performed on a Tecnai Osiris (FEI, USA) electron microscope operated at 200 kV and equipped with Super-X SDD high-sensitivity EDX spectrometer and on a JEM ARM200F cold FEG double aberration corrected electron microscope operated at 200 kV and equipped with a large solid angle CENTURIO EDX detector, Gatan GIF Quantum and ORIUS CCD camera. TEM samples were prepared by dropping of UCNP aqueous dispersion onto Cu holey carbon grids. As-synthesized UCNPs were dispersed in hexane and TEM samples were prepared in the same way.

5.6 Luminescent microscope

A diode laser (ATC-C4000-200-AMF-975, Semiconductor devices, Russia) operating at wavelength 975 nm delivered the excitation light to the sample plane of an inverted epi-luminescence microscope (Motic AE30-31, China). The excitation beam was filtered with a laser line filter (Semrock, USA) and shaped to converge at the back focal plane of an objective lens (4×, NA 0.1, Motic, China), which was used for both bright-field and UCNP assisted photoluminescent imaging at 800 nm. The sample plane was imaged using a 4.2 megapixels sCMOS CCD camera (Gen II, Photonic Science, GB). Glass slide with water drop contain *D. magna* used as the specimens for optical microscopy procedures.

Acknowledgements

Electronic Supplementary Material: Supplementary material (TEM images, EDX mapping, Schematic views of structural model, Luminescent images of aquatic organism, Phase diagram, XRD) is available in the online version of this article at https://doi.org/10.1007/s12274-020-3163-4.

References

[1] Deng, R. R.; Qin, F.; Chen, R. F.; Huang, W.; Hong, M. H.; Liu, X. G. Temporal full-colour tuning through non-steady-state upconversion. *Nat. Nanotechnol.* **2015**, *10*, 237–242.

[2] Generalova, A. N.; Chichkov, B. N.; Khaydukov, E. V. Multicomponent nanocrystals with anti-stokes luminescence as contrast agents for modern imaging techniques. *Adv. Colloid Interface Sci.* **2017**, *245*, 1–19.

[3] Chen, G. Y.; Qiu, H. L.; Prasad, P. N.; Chen, X. Y. Upconversion nanoparticles: Design, nanochemistry, and applications in theranostics. *Chem. Rev.* **2014**, *114*, 5161–5214.

[4] Li, H.; Tan, M. L.; Wang, X.; Li, F.; Zhang, Y. Q.; Zhao, L. L.; Yang, C. H.; Chen, G. Y. Temporal multiplexed *in vivo* upconversion imaging. *J. Am. Chem. Soc.* **2020**, *142*, 2023–2030.

[5] Cheng, L.; Wang, C.; Liu, Z. Upconversion nanoparticles and their composite nanostructures for biomedical imaging and cancer therapy. *Nanoscale* **2013**, *5*, 23–37.

[6] Mironova, K. E.; Khochenkov, D. A.; Generalova, A. N.; Rocheva, V. V.; Sholina, N. V.; Nechaev, A. V.; Semchishen, V. A.; Deyev, S. M.; Zvyagin, A. V.; Khaydukov, E. V. Ultraviolet phototoxicity of upconversion nanoparticles illuminated with near-infrared light. *Nanoscale* **2017**, *9*, 14921–14928.

[7] Zhu, X. J.; Feng, W.; Chang, J.; Tan, Y. W.; Li, J. C.; Chen, M.; Sun, Y.; Li, F. Y. Temperature-feedback upconversion nanocomposite for accurate photothermal therapy at facile temperature. *Nat. Commun.* **2016**, *7*, 10437.

[8] Kumar, M.; Zhang, P. Highly sensitive and selective label-free optical detection of mercuric ions using photon upconverting nanoparticles. *Biosens. Bioelectron.* **2010**, *25*, 2431–2435.

[9] Green, K. K.; Wirth, J.; Lim, S. F. Nanoplasmonic upconverting nanoparticles as orientation sensors for single particle microscopy. *Sci. Rep.* **2017**, *7*, 762.

[10] Khaydukov, E. V.; Rocheva, V. V.; Mironova, K. E.; Generalova, A. N.; Nechaev, A. V.; Semchishen, V. A.; Panchenko, V. Y. Biocompatible upconversion ink for hidden anticounterfeit labeling. *Nanotechnol. Russ.* **2015**, *10*, 904–909.

[11] Meruga, J. M.; Cross, W. M.; Stanley May, P.; Luu, Q.; Crawford, G. A.; Kellar, J. J. Security printing of covert quick response codes using upconverting nanoparticle inks. *Nanotechnology* **2012**, *23*, 395201.

[12] Hao, S. W.; Shang, Y. F.; Li, D. Y.; Ågren, H.; Yang, C. H.; Chen, G. Y. Enhancing dye-sensitized solar cell efficiency through broadband near-infrared upconverting nanoparticles. *Nanoscale* **2017**, *9*, 6711–6715.

[13] Shang, Y. F.; Hao, S. W.; Yang, C. H.; Chen, G. Y. Enhancing solar cell efficiency using photon upconversion materials. *Nanomaterials* **2015**, *5*, 1782–1809.

[14] Rocheva, V. V.; Koroleva, A. V.; Savelyev, A. G.; Khaydukov, K. V.; Generalova, A. N.; Nechaev, A. V.; Guller, A. E.; Semchishen, V. A.; Chichkov, B. N.; Khaydukov, E. V. High-resolution 3D photopolymerization assisted by upconversion nanoparticles for rapid prototyping applications. *Sci. Rep.* **2018**, *8*, 3663.

[15] Chen, Y. W.; Zhang, J. M.; Liu, X.; Wang, S.; Tao, J.; Huang, Y. L.; Wu, W. B.; Li, Y.; Zhou, K.; Wei, X. W. et al. Noninvasive *in vivo* 3D bioprinting. *Sci. Adv.* **2020**, *6*, eaba7406.

[16] Generalova, A. N.; Kochneva, I. K.; Khaydukov, E. V.; Semchishen, V. A.; Guller, A. E.; Nechaev, A. V.; Shekhter, A. B.; Zubov, V. P.; Zvyagin, A. V.; Deyev, S. M. Submicron polyacrolein particles *in situ* embedded with upconversion nanoparticles for bioassay. *Nanoscale* **2015**, *7*, 1709–1717.

[17] Nadort, A.; Zhao, J. B.; Goldys, E. M. Lanthanide upconversion luminescence at the nanoscale: Fundamentals and optical properties. *Nanoscale* **2016**, *8*, 13099–13130.

[18] Buchinskaya, I. I.; Karimov, D. N.; Zakalyukin, R. M.; Gali, S. Vapor-phase growth of CdF_2 whiskers in the CdF_2-GaF_3 system. *Crystallogr. Rep.* **2007**, *52*, 170–173.

[19] Yang, D. D.; Chen, D. D.; He, H. L.; Pan, Q. W.; Xiao, Q. L.; Qiu, J. R.; Dong, G. P. Controllable phase transformation and mid-infrared emission from Er^{3+}-doped hexagonal-/cubic-$NaYF_4$ nanocrystals. *Sci. Rep.* **2016**, *6*, 29871.

[20] Wang, L. Y.; Li, Y. D. $Na(Y_{1.5}Na_{0.5})F_6$ single-crystal nanorods as multicolor luminescent materials. *Nano Lett.* **2006**, *6*, 1645–1649.

[21] Yan, Z. J.; Chrisey, D. B. Pulsed laser ablation in liquid for micro/nanostructure generation. *J. Photochem. Photobiol. C* **2012**, *13*, 204–223.

[22] Kabashin, A. V.; Delaporte, P.; Pereira, A.; Grojo, D.; Torres, R.; Sarnet, T.; Sentis, M. Nanofabrication with pulsed lasers. *Nanoscale Res. Lett.* **2010**, *5*, 454–463.

[23] Barchanski, A.; Funk, D.; Wittich, O.; Tegenkamp, C.; Chichkov, B. N.; Sajti, C. L. Picosecond laser fabrication of functional gold–antibody nanoconjugates for biomedical applications. *J. Phys. Chem. C* **2015**, *119*, 9524–9533.

[24] Mafuné, F.; Kohno, J. Y.; Takeda, Y.; Kondow, T.; Sawabe, H. Structure and stability of silver nanoparticles in aqueous solution produced by laser ablation. *J. Phys. Chem. B* **2000**, *104*, 8333–8337.

[25] Usui, H.; Shimizu, Y.; Sasaki, T.; Koshizaki, N. Photoluminescence of ZnO nanoparticles prepared by laser ablation in different surfactant solutions. *J. Phys. Chem. B* **2005**, *109*, 120–124.

[26] Katsuki, D.; Sato, T.; Suzuki, R.; Nanai, Y.; Kimura, S.; Okuno, T. Red luminescence of Eu^{3+} doped ZnO nanoparticles fabricated by laser ablation in aqueous solution. *Appl. Phys. A* **2012**, *108*, 321–327.

[27] Sasaki, T.; Liang, C.; Nichols, W. T.; Shimizu, Y.; Koshizaki, N. Fabrication of oxide base nanostructures using pulsed laser ablation in aqueous solutions. *Appl. Phys. A* **2004**, *79*, 1489–1492.

[28] Park, G. S.; Kim, K. M.; Mhin, S. W.; Eun, J. W.; Shim, K. B.; Ryu, J. H.; Koshizaki, N. Simple route for $Y_3Al_5O_{12}$:Ce^{3+} colloidal nanocrystal via laser ablation in deionized water and its luminescence. *Electrochem. Solid State Lett.* **2008**, *11*, J23.

[29] Edmonds, A. M.; Sobhan, M. A.; Sreenivasan, V. K. A.; Grebenik, E. A.; Rabeau, J. R.; Goldys, E. M.; Zvyagin, A. V. Nano-ruby: A promising fluorescent probe for background-free cellular imaging. *Part. Part. Syst. Char.* **2013**, *30*, 506–513.

[30] Nee, C. H.; Yap, S. L.; Tou, T. Y.; Chang, H. C.; Yap, S. S. Direct synthesis of nanodiamonds by femtosecond laser irradiation of ethanol. *Sci. Rep.* **2016**, *6*, 33966.

[31] Maurer, E.; Barcikowski, S.; Gökce, B. Process chain for the fabrication of nanoparticle polymer composites by laser ablation synthesis. *Chem. Eng. Technol.* **2017**, *40*, 1535–1543.

[32] Tamaki, Y.; Asahi, T.; Masuhara, H. Nanoparticle formation of vanadyl phthalocyanine by laser ablation of its crystalline powder in a poor solvent. *J. Phys. Chem. A* **2002**, *106*, 2135–2139.

[33] Scaramuzza, S.; Agnoli, S.; Amendola, V. Metastable alloy nanoparticles, metal-oxide nanocrescents and nanoshells generated by laser ablation in liquid solution: Influence of the chemical environment on structure and composition. *Phys. Chem. Chem. Phys.* **2015**, *17*, 28076–28087.

[34] Onodera, Y.; Nunokawa, T.; Odawara, O.; Wada, H. Upconversion properties of Y_2O_3:Er,Yb nanoparticles prepared by laser ablation in water. *J. Lumin.* **2013**, *137*, 220–224.

[35] Ikehata, T.; Onodera, Y.; Nunokawa, T.; Hirano, T.; Ogura, S.; Kamachi, T.; Odawara, O.; Wada, H. Photodynamic therapy using upconversion nanoparticles prepared by laser ablation in liquid. *Appl. Surf. Sci.* **2015**, *348*, 54–59.

[36] Gemini, L.; Schmitz, T.; Kling, R.; Barcikowski, S.; Gökce, B. Upconversion nanoparticles synthesized by ultrashort pulsed laser ablation in liquid: Effect of the stabilizing environment. *ChemPhysChem* **2017**, *18*, 1210–1216.

[37] Liang, X.; Wang, X.; Zhuang, J.; Peng, Q.; Li, Y. Synthesis of $NaYF_4$ nanocrystals with predictable phase and shape. *Adv. Funct. Mater.* **2007**, *17*, 2757–2765.

[38] Wilhelm, S. Perspectives for upconverting nanoparticles. *ACS Nano* **2017**, *11*, 10644–10653.

[39] Holmberg, K.; Jönsson, B.; Kronberg, B.; Lindman, B. *Surfactants and Polymers in Aqueous Solution*; 2nd ed. Wiley & Sons, Ltd: Chichester, 2002.

[40] Alyatkin, S.; Asharchuk, I.; Khaydukov, K.; Nechaev, A.; Lebedev, O.; Vainer, Y.; Semchishen, V.; Khaydukov, E. The influence of energy migration on luminescence kinetics parameters in upconversion nanoparticles. *Nanotechnology* **2017**, *28*, 035401.

[41] Zhu, X. S.; Chang, Y., Chen, Y. S. Toxicity and bioaccumulation of TiO_2 nanoparticle aggregates in *Daphnia magna*. *Chemosphere* **2010**, *78*, 209–215.

[42] Fedorov, P. P.; Sobolev, B. P.; Belov, S. F. Fusibility diagram of the system NaF-YF_3, and the cross-section $Na_{0.4}Y_{0.6}F_{2.2}$-YOF. *Inorg. Mater.* **1979**, *15*, 640–643.

[43] Perera, S. S.; Amarasinghe, D. K.; Dissanayake, K. T.; Rabuffetti, F. A. Average and local crystal structure of β-Er:Yb:$NaYF_4$ upconverting nanocrystals probed by X-ray total scattering. *Chem. Mater.* **2017**, *29*, 6289–6297.

[44] Blistanov, A. A.; Chernov, S. P.; Karimov, D. N.; Ouvarova, T. V. Peculiarities of the growth of disordered Na,R-fluorite (R=Y, Ce–Lu) single crystals. *J. Cryst. Growth* **2002**, *237–239*, 899–903.

[45] Pin, M. W.; Park, E. J.; Choi, S.; Kim, Y. I.; Jeon, C. H.; Ha, T. H.; Kim, Y. H. Atomistic evolution during the phase transition on a metastable single $NaYF_4$:Yb,Er upconversion nanoparticle. *Sci. Rep.* **2018**, *8*, 2199.

[46] Chichkov, B. N.; Momma, C.; Nolte, S.; von Alvensleben, F.; Tünnermann, A. Femtosecond, picosecond and nanosecond laser ablation of solids. *Appl. Phys. A* **1996**, *63*, 109–115.

[47] Rafiei Miandashti, A.; Khosravi Khorashad, L.; Govorov, A. O.; Kordesch, M. E.; Richardson, H. H. Time-resolved temperature-jump measurements and theoretical simulations of nanoscale heat transfer using $NaYF_4$: Yb^{3+}: Er^{3+} upconverting nanoparticles. *J. Phys. Chem. C* **2019**, *123*, 3770–3780.

[48] Liu, H. Q.; Han, J. K.; McBean, C.; Lewis, C. S.; Routh, P. K.; Cotlet, M.; Wong, S. S. Synthesis-driven, structure-dependent optical behavior in phase-tunable $NaYF_4$:Yb,Er-based motifs and associated heterostructures. *Phys. Chem.* **2017**, *19*, 2153–2167.

[49] Liao, H. G.; Cui, L. K.; Whitelam, S.; Zheng, H. M. Real-time imaging of Pt_3Fe nanorod growth in solution. *Science* **2012**, *336*, 1011–1014.

[50] Ye, S. R.; Chen, Z. F.; Ha, Y. C.; Wiley, B. J. Real-time visualization of diffusion-controlled nanowire growth in solution. *Nano Lett.* **2014**, *14*, 4671–4676.

[51] Khaydukov, E. V.; Mironova, K. E.; Semchishen, V. A.; Generalova, A. N.; Nechaev, A. V.; Khochenkov, D. A.; Stepanova, E. V.; Lebedev, O. I.; Zvyagin, A. V.; Deyev, S. M. M. et al. Riboflavin photoactivation by upconversion nanoparticles for cancer treatment. *Sci. Rep.* **2016**, *6*, 35103.

[52] *Dyomics Catalogue Fluorescent Dyes for Bioanalytical and Hightech Applications,* 2017 [Online]. https://dyomics.com/en/products/red-excitation/dy-631 (Accessed Jul 1, 2020).